Supplement of Geosci. Model Dev., 16, 851–867, 2023
https://doi.org/10.5194/gmd-16-851-2023-supplement

Geoscientific Model Development
Open Access

Supplement of

Cell tracking of convective rainfall: sensitivity of climate-change signal to tracking algorithm and cell definition (Cell-TAO v1.0)

Edmund P. Meredith et al.

Correspondence to: Edmund P. Meredith (edmund.meredith@met.fu-berlin.de)

1 Supporting Figures

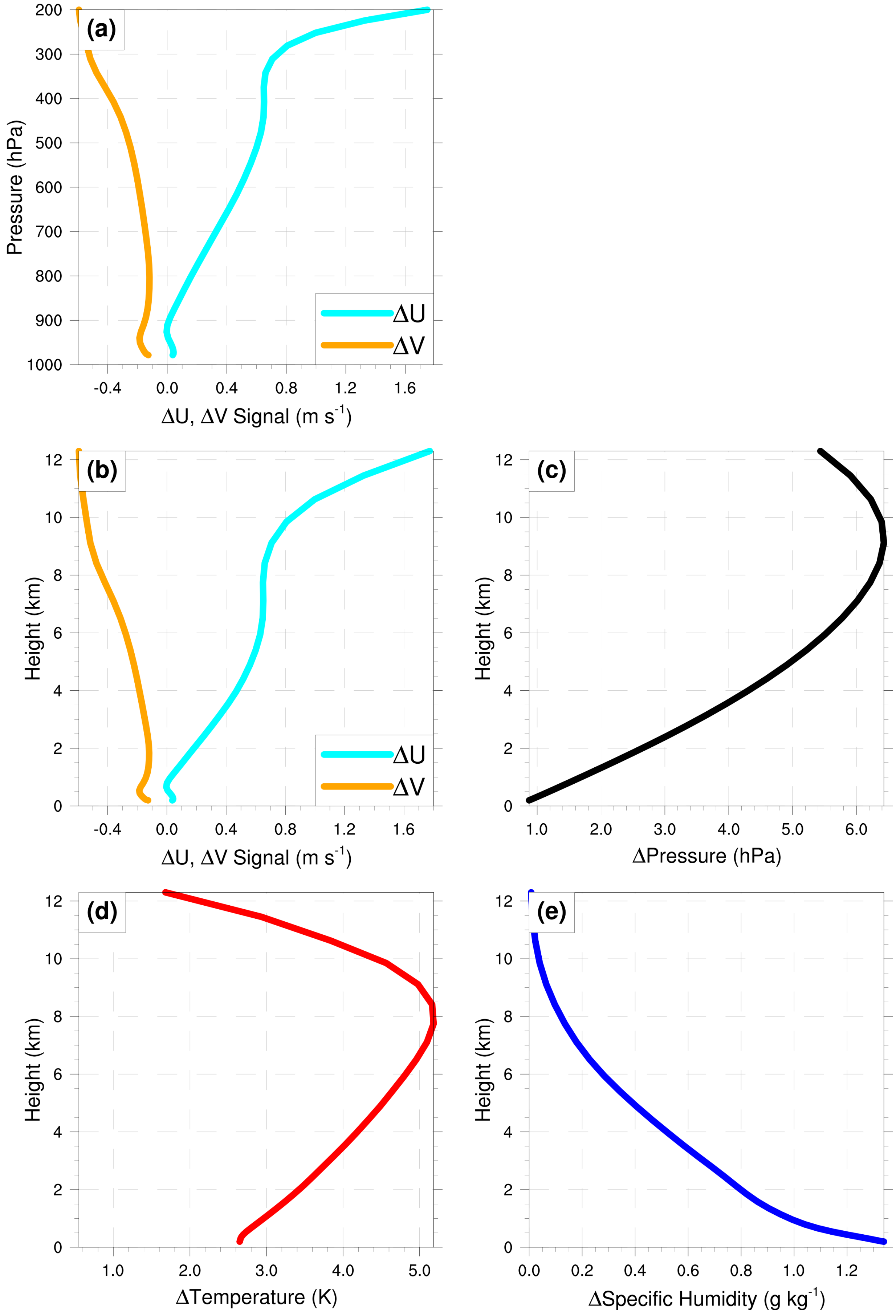

Figure S1: Climate-change signals of (a) eastward (U) and northward (V) winds on pressure levels, (b) eastward (U) and northward (V) winds, (c) pressure, (d) temperature and (e) humidity all on height levels added to the initial and boundary conditions of the 0.11° PGW simulations. The unequal vertical warming signal (d) implies a change in lapse rate, while the vertically increasing zonal wind shear (a, b) and hence vertical baroclinicty gradient implies horizontal temperature gradients increasing with height. The signal is computed based on an area average over the 0.11° domain.

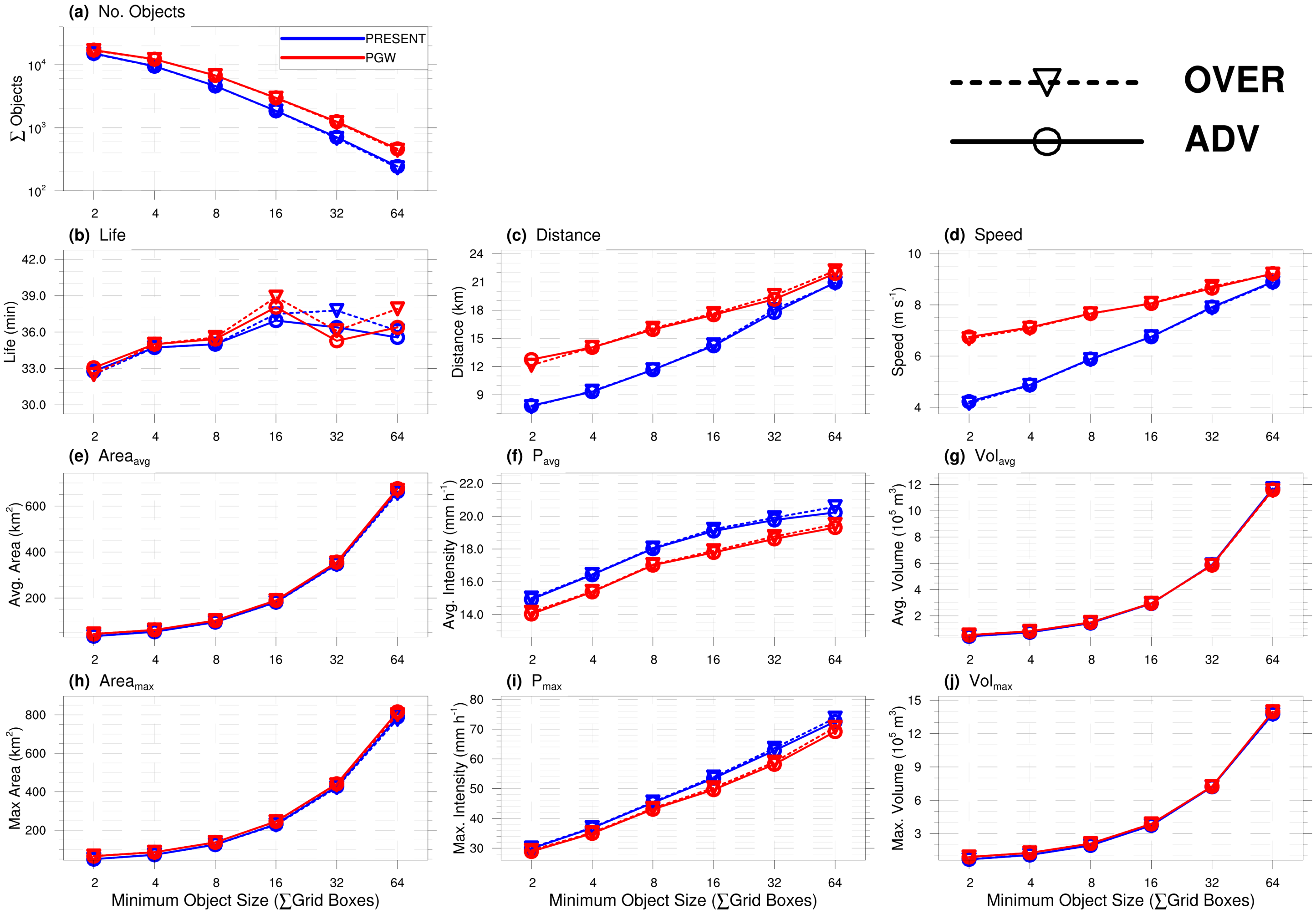

Figure S2: Different object properties in present and future climates as a function of the object's minimum-area criterion A_{min}, for both algorithms. These are the values underlying the change signals shown in Fig. 3 of the main manuscript. A_{min} is defined in terms of grid boxes, with each grid box having an area of $\sim$7.7 km^2. The A_{min} range thus spans approximately 15 to 493 km^2.

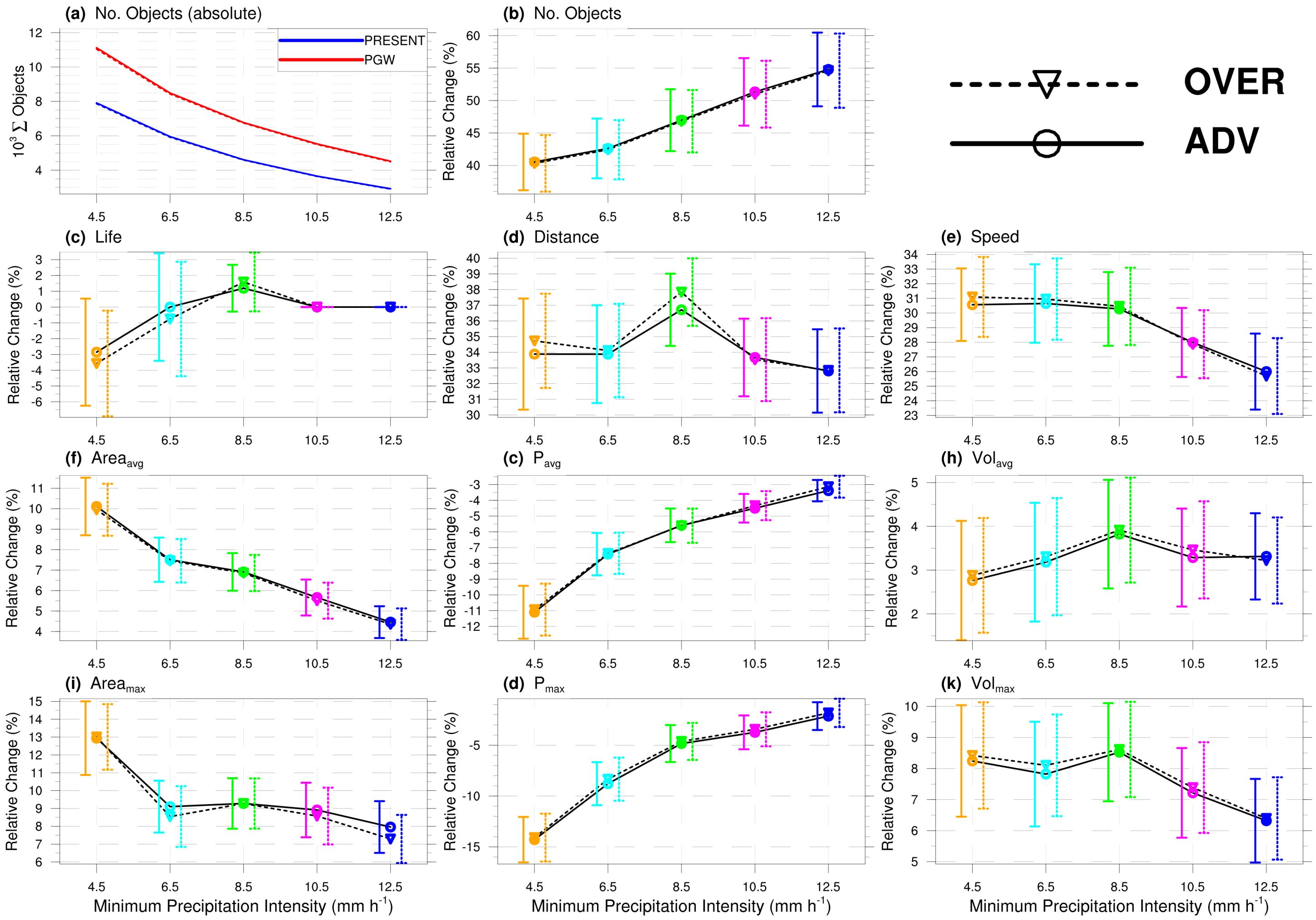

Figure S3: Climate-change signals of all object properties and N_{obj} as a function of the object's minimum-precipitation-intensity criterion P_{min}, for both algorithms. This plot includes the change signals for all object properties, and thus complements the change signals shown for selected properties in Fig. 4 of the main manuscript. Change signals which are different with statistical significance at the 0.95 level can be identified based on non-overlapping CIs (see Methods in main manuscript), seen as vertical solid (advection) or dashed (overlap) lines. P_{min} is shown as the equivalent hourly rate based on 5 min intensities. In panel (a), the values for the number of objects are shown (i.e. the sample sizes). The values underlying the change signals can be seen in Fig. S4

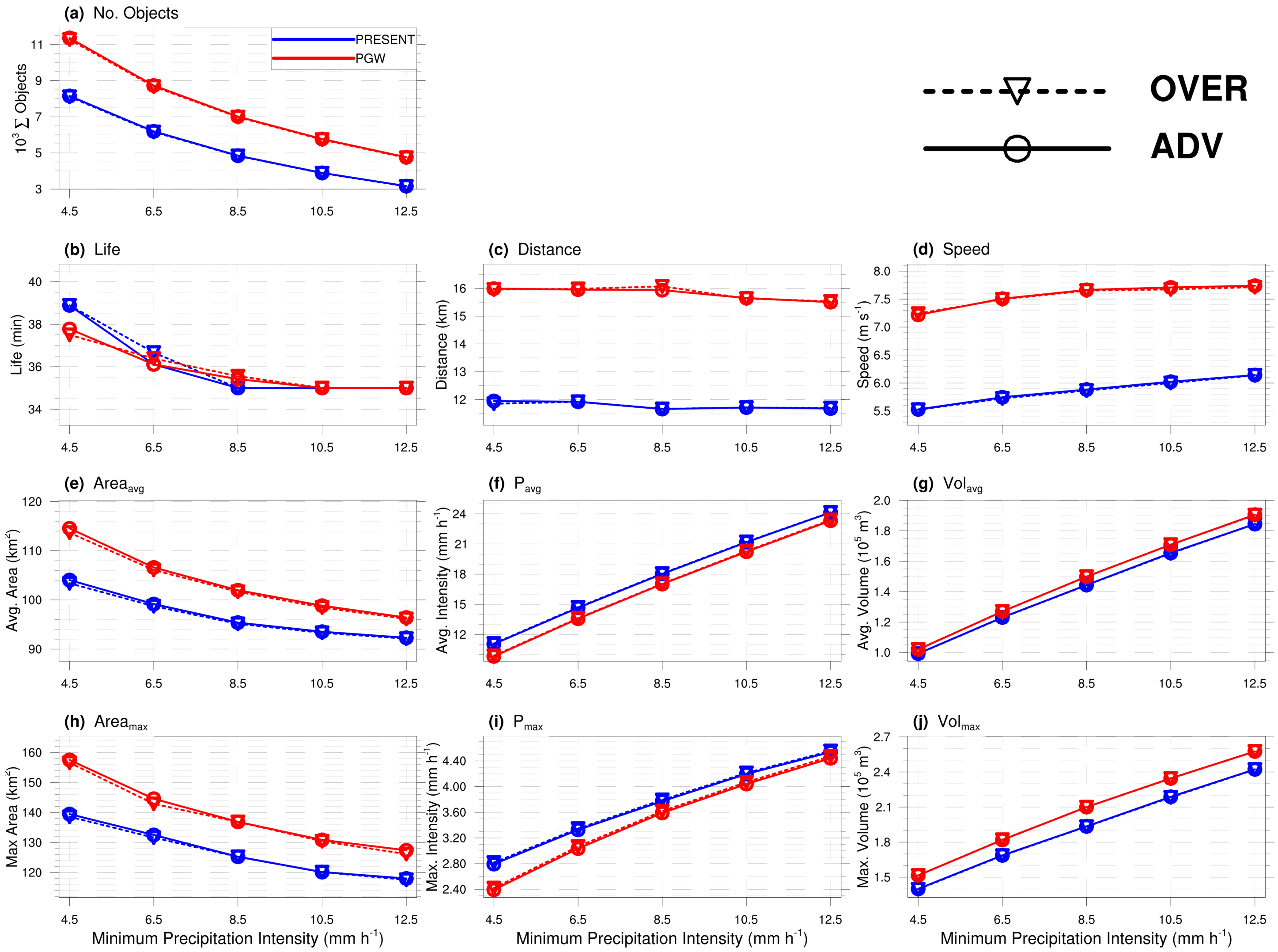

Figure S4: Different object properties in present and future climates as a function of the object's minimum-precipitation criterion P_{min}, for both algorithms. These are the values underlying the change signals shown in Fig. 4 of the main manuscript and Fig. S3. P_{min} is shown as the equivalent hourly rate based on 5 min intensities.

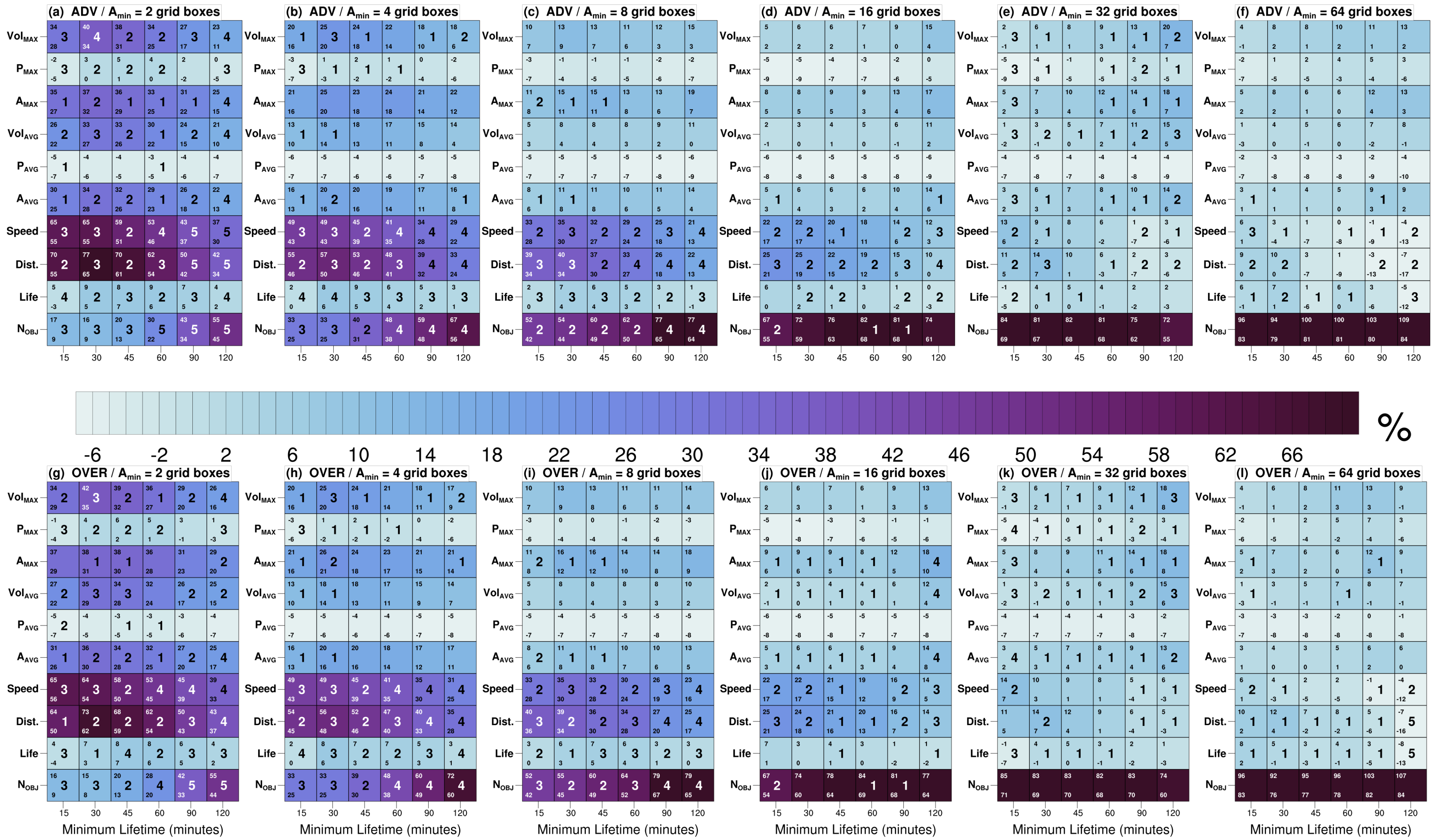

Figure S5: Climate-change signals of all object properties and N_{obj}, as a function of the object's minimum-lifetime criterion T_{min}, for both algorithms. Confidence intervals (computed as described in main manuscript) are given in the left-hand corners of each box. The number in the centre of each box (if present) denotes how many of the other T_{min} thresholds have change signals which are significantly different to the box in question (maximum = 5, $\alpha = 0.95$). For example, in the bottom row of panel (g) – OVER, $A_{min} = 2$ grid boxes, N$_{OBJ}$ – the value 3 is present at $T_{min} = 15$ minutes; this means 3 of the remaining 5 climate-changes signals (N_{OBJ}; T_{min} = 30-, 45-, 60-, 90-, 120- minutes) have a statistically significant difference to the box in question. There are no statistically significant differences between the algorithms. The results shown here include all six values of A_{min}, and thus complement the three values of A_{min} shown in the main manuscript.

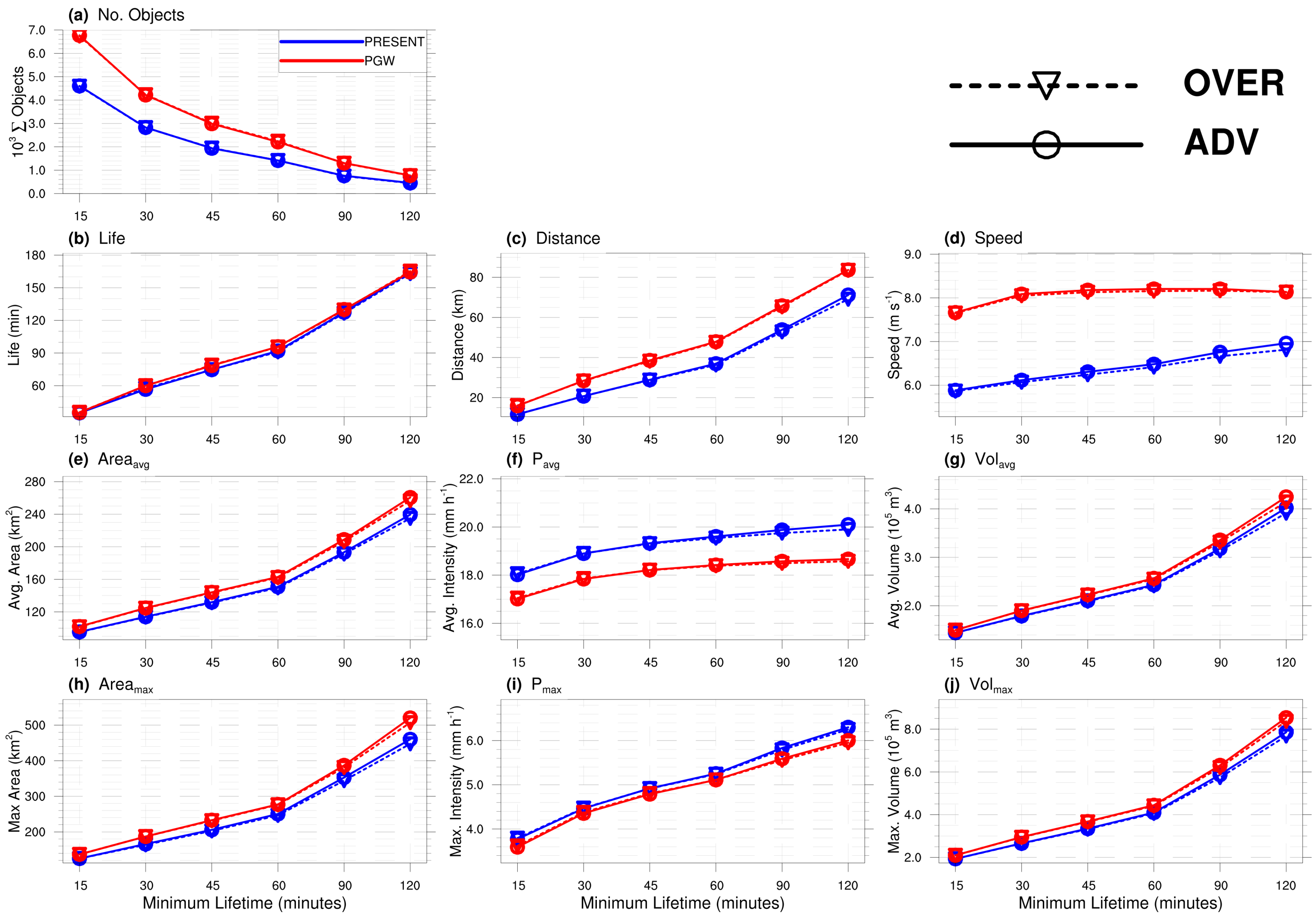

Figure S6: Different object properties, and N_{obj}, in present and future climates as a function of the object's minimum-lifetime criterion (T_{min}). In the figure, A_{min} has a value of 8 grid boxes and P_{min} a value of 8.5 mm h^{-1}, i.e. the reference setup values. The figure thus shows the values underlying the change signals in Fig. 6 (b, e) in the main manuscript and Fig. S5 (c, i) in this document.

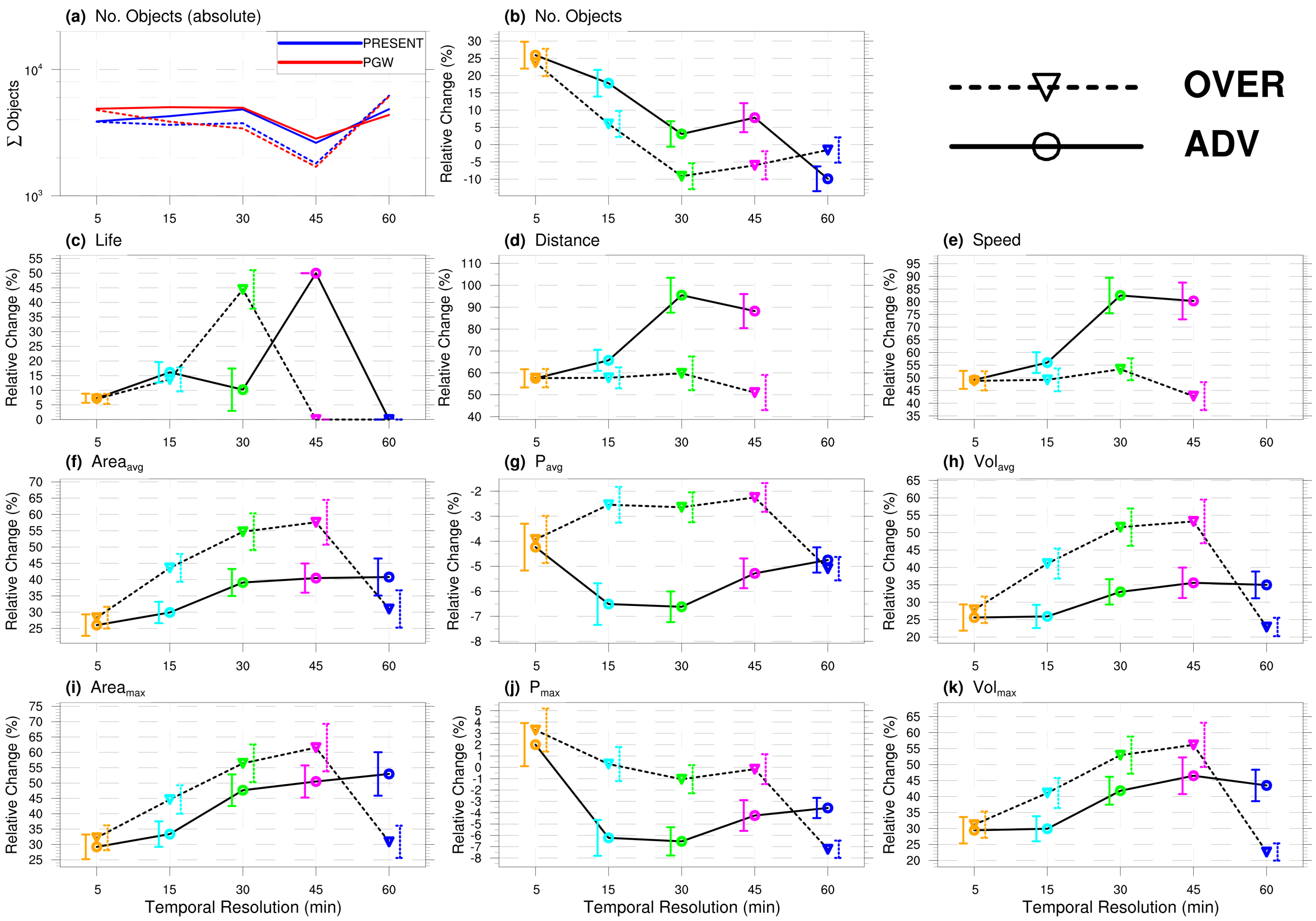

Figure S7: Sensitivity of climate-change signal to temporal resolution of precipitation data. As in Fig. 8 of the main manuscript, except using A_{min} = **2 grid boxes** instead. To note is that the difference between the tracking algorithms *increases* compared to when A_{min} = 8 grid boxes (as in the main manuscript).

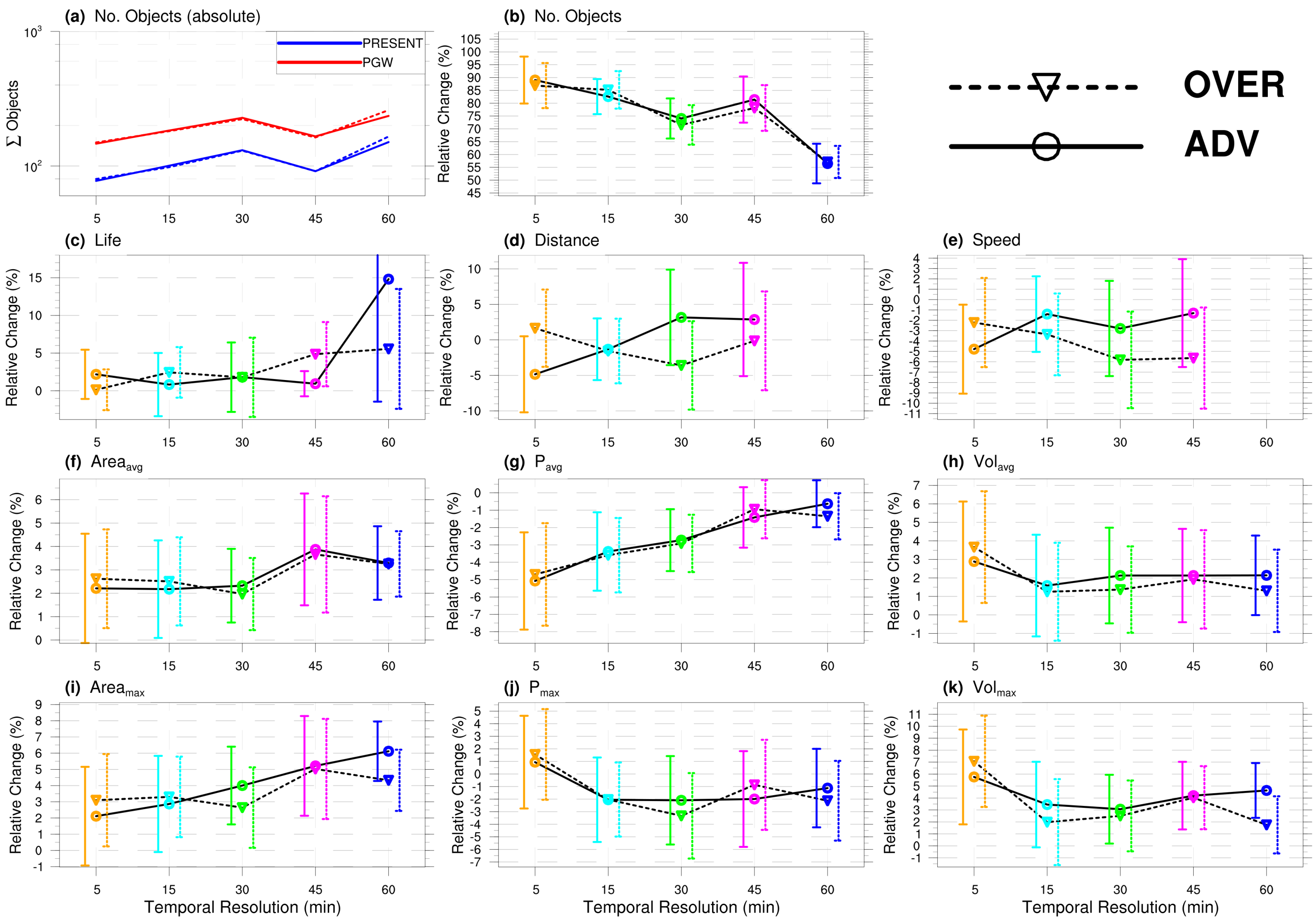

Figure S8: Sensitivity of climate-change signal to temporal resolution of precipitation data. As in Fig. 8 of the main manuscript, except using A_{min} = **64 grid boxes** instead. To note is that the difference between the tracking algorithms *decreases* compared to when A_{min} = 8 grid boxes (as in the main manuscript).

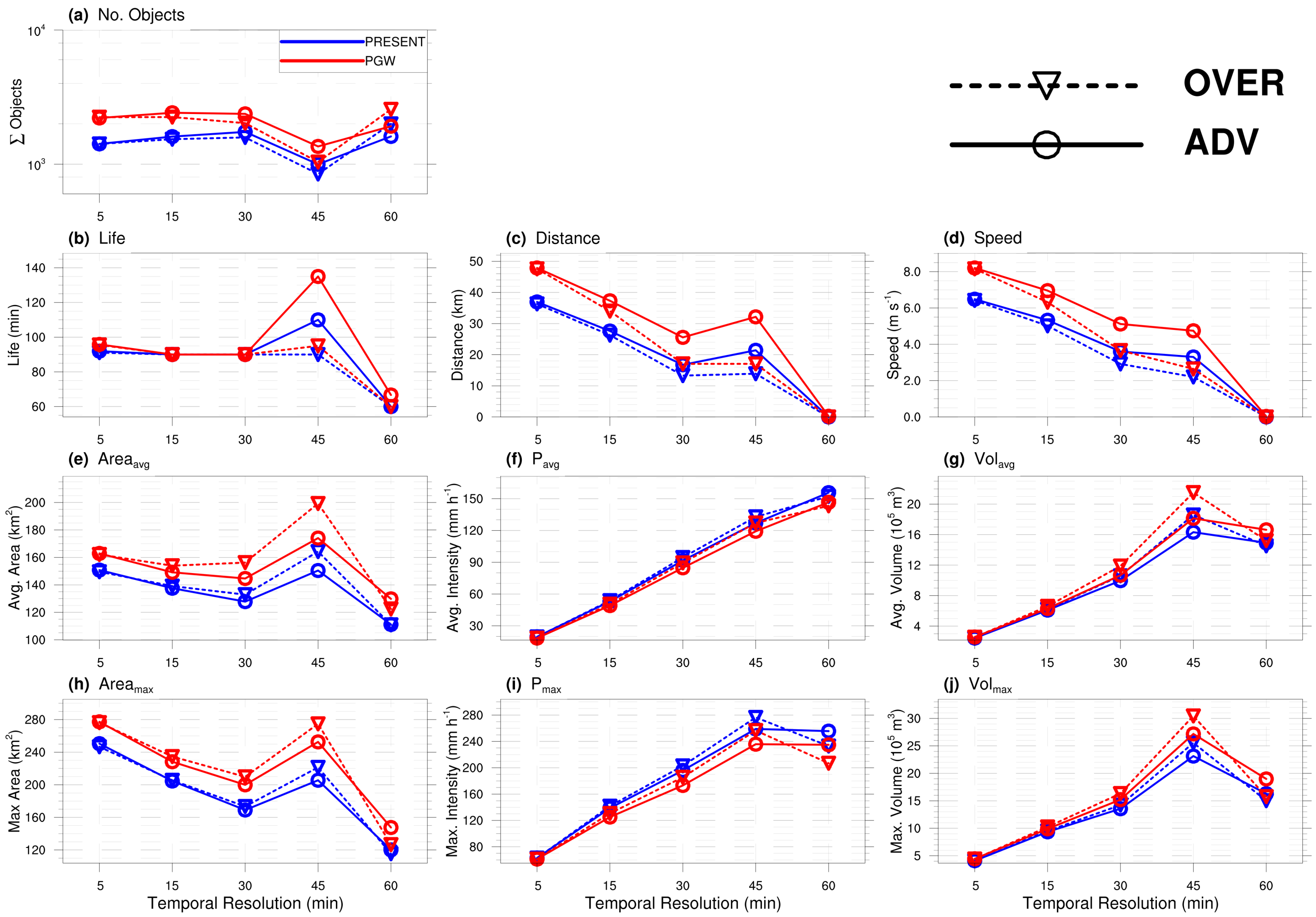

Figure S9: Different object properties in present and future climates as a function of the precipitation data's temporal resolution. The threshold criteria are as in the reference settings (A_{min} = 8 grid boxes, P_{min} = 8.5 mm h^{-1} and T_{min} = 15 min). Shown are the values which underlie the change signals shown in Fig. 8 of the main manuscript.

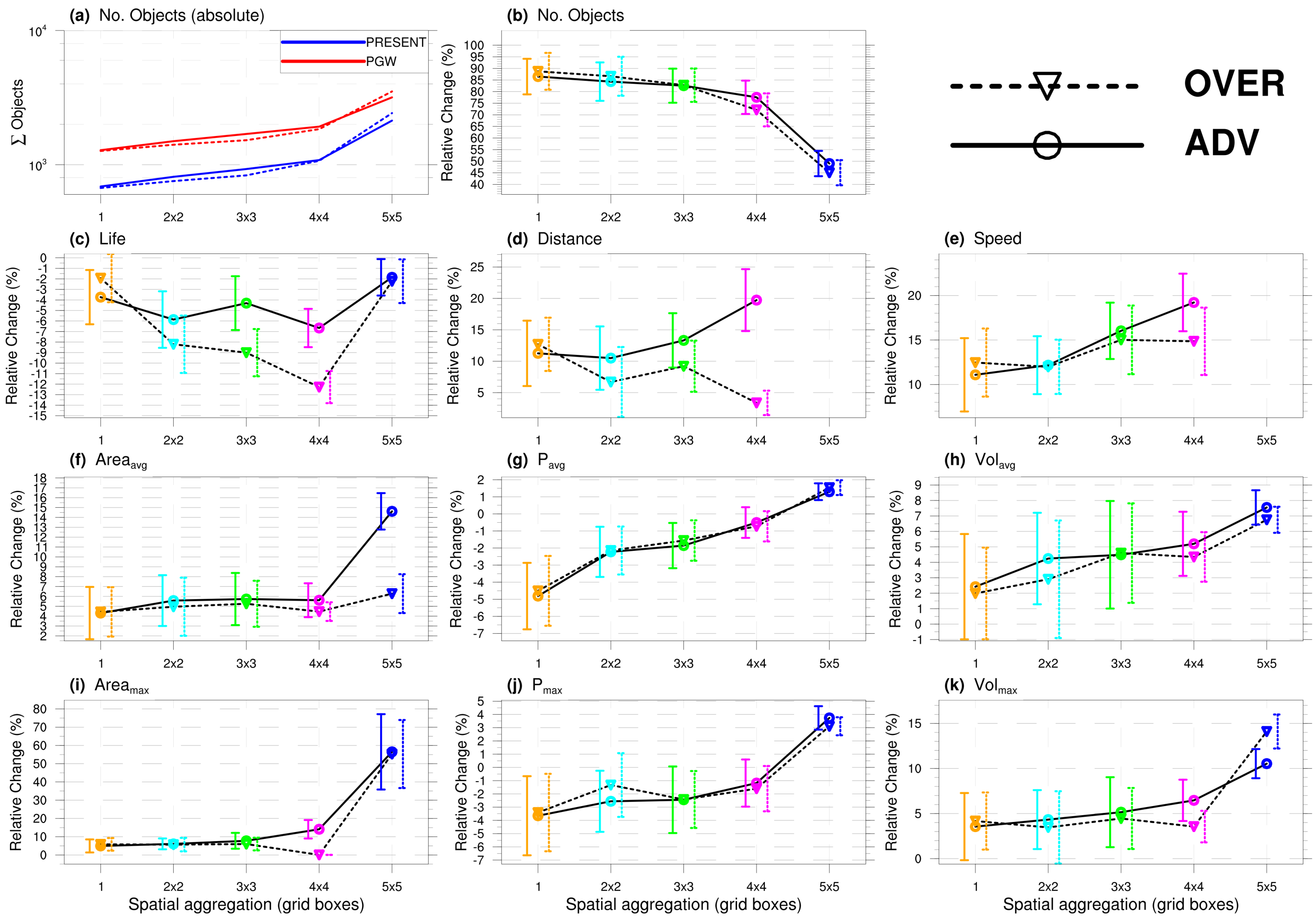

Figure S10: Climate-change signals of different object properties as a function of the precipitation data's spatial resolution, for both algorithms (A_{min}, P_{min} and T_{min} are kept at their reference values). The spatial resolution (x-axis) is defined based on grid boxes from the native (0.025°) grid, e.g. the 5x5 value means that the native grid was aggregated over a square of 25 grid boxes. Change signals which are different with statistical significance at the 0.95 level can be identified based on non-overlapping CIs (see Methods), seen as vertical solid (advection) or dashed (overlap) lines. In panel (a), the numbers of objects are shown (i.e. the sample sizes). For object properties with a median value of zero in the present climate, a %-change signal cannot be defined, hence the missing values for the 5x5-cells distance and speed. Note that to ensure a fair comparison, only objects with an area equivalent to at least 5x5 grid boxes on the 0.025° grid are considered; each grid box has an area of ∼7.7 km^2.

2 Supporting discussion

2.1 Tests with other climate simulations

In Fig. S11, the reference settings have been used to repeat the tracking on a longer set of simulations, with both the ADV and OVER algorithms. These simulations comprise 30 summers from 1970-1999 and 2070-2099 under the RCP8.5 scenario, downscaled first over the EURO-CORDEX domain to 0.11° and then further to 0.02° over a smaller domain covering parts of western Germany, Benelux and parts of France. The simulations are described in the publications Meredith et al. (2018, 2019, 2021), where maps of the simulation domain can also be seen. The aim of this tracking, as mentioned in the main manuscript, is to see if the conclusion that the choice of tracking algorithm has no significant effect on the climate-change signal (assuming the precipitation data is of sufficiently high temporal resolution) holds over a longer set of climate-change simulations. It could be speculated, for example, that the result in the main manuscript, i.e. that the tracking algorithm didn't affect the climate-change signal, is influenced by the particular set of weather situations which were present during the 14-day test period. If this were the case, then a longer set of climate simulations – which would naturally include a much larger set of weather situations – might be expected to reveal differences between the tracking algorithms. As can be seen in Fig. S11, in the climate-length simulations, the choice of tracking algorithm does not have a significant impact on the climate-change signal (note that here the precipitation data have a 5-minute temporal resolution). The one exception is for the object-lifetime metric. It is worth commenting here that the object lifetime is the only fully discretized object property – in steps of 5 min. For this reason, small shifts in the distribution of object lifetimes can, when considering the median, have a large impact on the magnitude of the climate-change signal, thus producing apparently large differences in the climate-change signals between the two algorithms. This can be seen in Fig. S12a, where a small increase in the quantile often leads to a dramatic difference in the climate-change signals of the object-lifetime quantiles. A similar effect, though on a much smaller scale, can be seen in the distance metric (Fig. S12i) and in the low quantiles of the maximum area metric (Fig. S12e).

Readers may additionally ask why these simulations weren't taken as the basis for the entire study. One reason is the computational expense associated with testing the different object definitions and algorithms at climate timescales (30 summers, present and future). The main reason, however, is that the simulation domain (which can be viewed in the aforementioned publications) is of suboptimal size for considering a diverse range of convective situations. Specifically, the domain is too small to consider larger convective systems whose spatial extent could easily exceed the width or length of the domain. Additionally, objects which travel a long distance may not complete their life cycles within the domain boundaries, thus making them ineligible for consideration. Convective objects which (i) are not fully captured within the domain, (ii) begin their lives outside the domain, or (iii) end their lives outside the domain cannot be considered in the overall statistics because it is not possible to compute the object's properties when only data for a fraction of the object's life cycle or spatial extent is available. With the larger domain used in the main manuscript, this problem arises much less often.

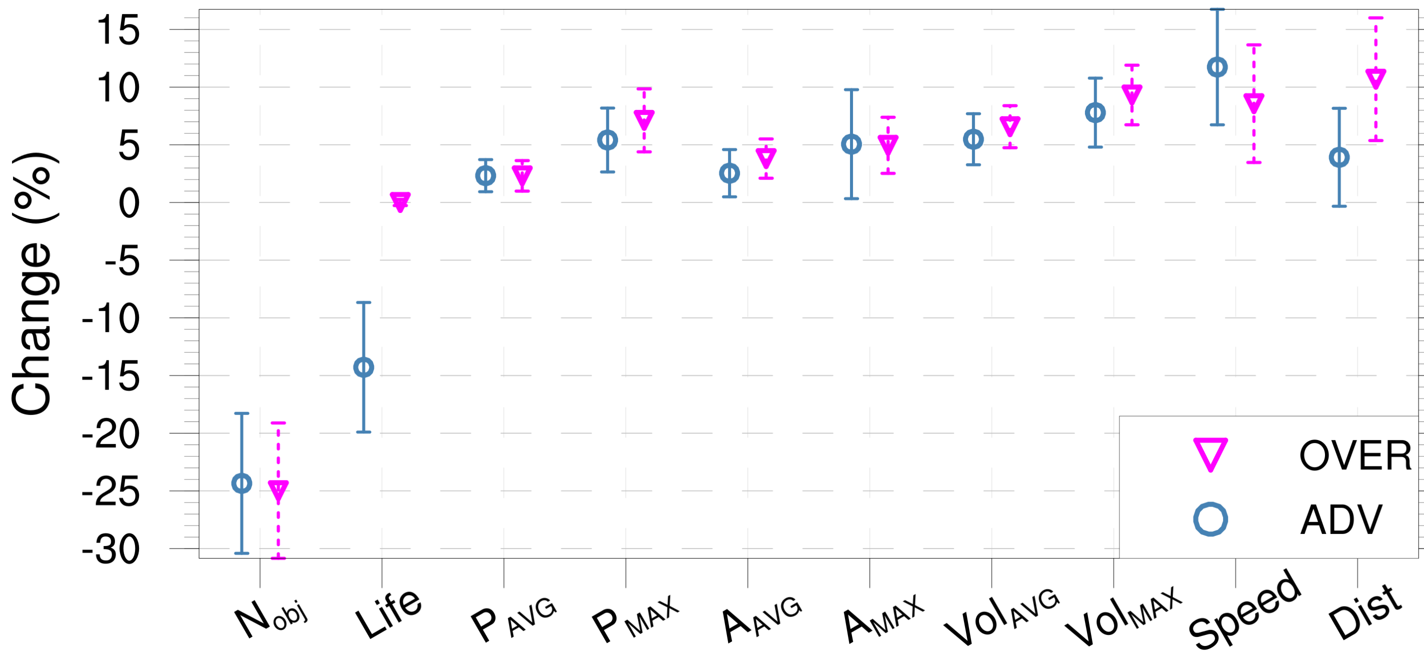

Figure S11: Climate-change signal for all object properties and N_{obj} based on the climate simulations used in Meredith et al. (2019). P_{min} and T_{min} take the reference values used in the present study. A_{min} closely matches the area of the reference A_{min} used in the present study, allowing for the fact that the simulations of Meredith et al. (2019) have a spatial resolution of 0.02°, as opposed to 0.025° in the present study. For each metric, change signals for each algorithm which are different from that of the other algorithm with statistical significance at the 0.95 level can be identified based on non-overlapping CIs (see Methods in main manuscript), seen as vertical solid (advection) or dashed (overlap) lines.

2.2 Climate-change signals for higher quantiles

In Figs. S13-S15, the analysis of Figs. 4-6 from the main manuscript has been repeated, except using the 0.9-quantile instead of the median. It can be seen that the relationships between the different object properties and the varying thresholds are similar, leading to the same conclusions. Also apparent is that the confidence intervals of the climate-change signals sometimes widen, resulting in a reduced number of statistically significant differences. A final point of note is that the magnitudes and range of the climate-change signals are often quite different to those of the median, as shown in the main manuscript. This is to be expected, as it is well known that higher quantiles of precipitation do not necessarily respond to warming in the same way as the mean (or median). As discussed in the main manuscript, the magnitude of the detected climate-change signals is anyway not pertinent to the aim of the analysis. Rather, the aim is assess *differences* in the climate-change signals and whether these are significant.

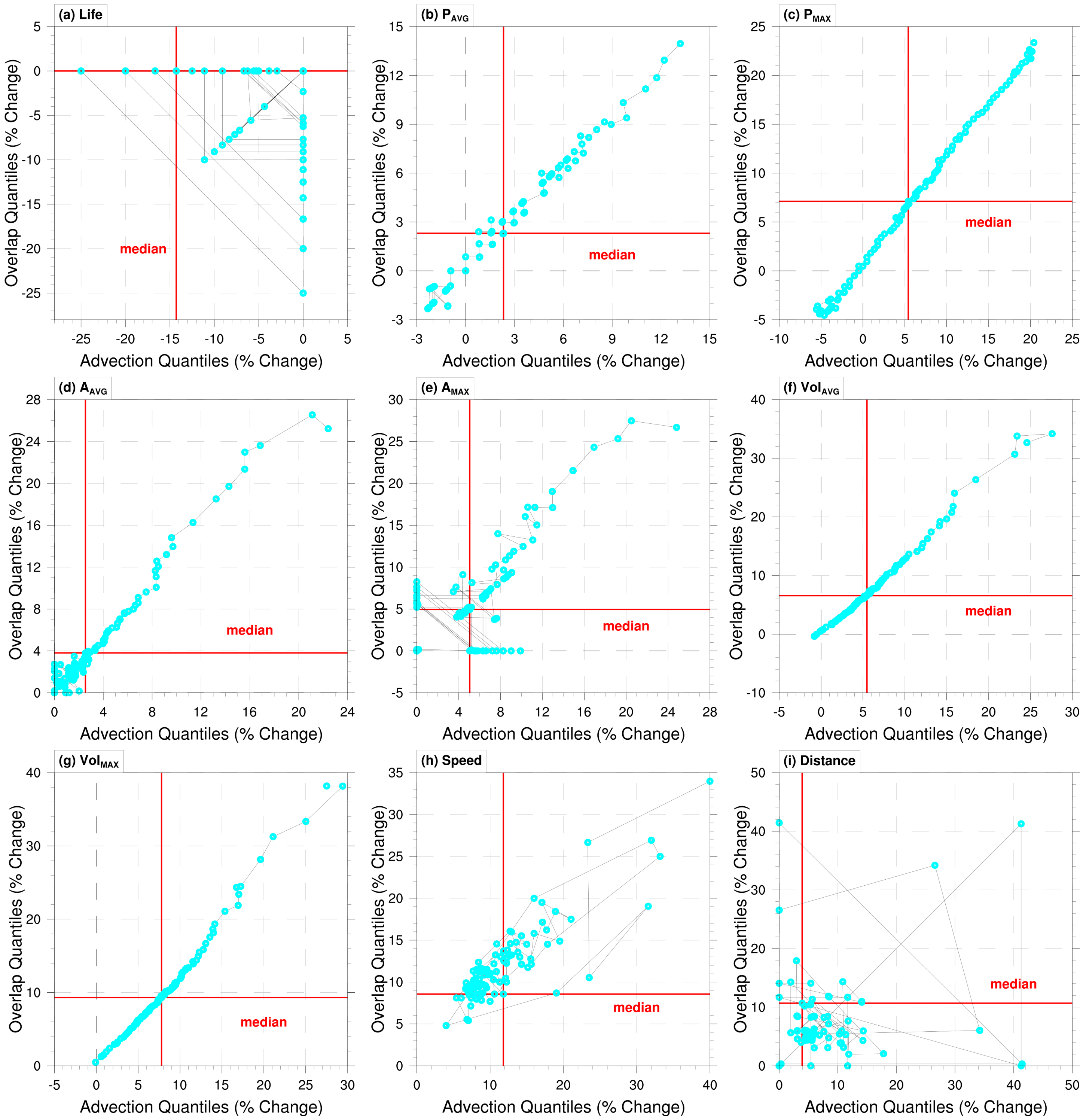

Figure S12: Quantile-Quantile plots of the climate-change signals in the overlap- (y-axis) and advection-based (x-axis) algorithms, for all object metrics. Quantiles from 0.01 to 0.99 in steps of 0.01 are shown. The red line denotes the 0.5 quantile, i.e. the median change signals shown in Fig. S11. Of note is panel (a), where the change in object lifetime is compared. Here, an increase to a quantile 0.01 higher is seen, in many cases, to lead to a dramatic difference in the magnitudes of the climate-change signals.

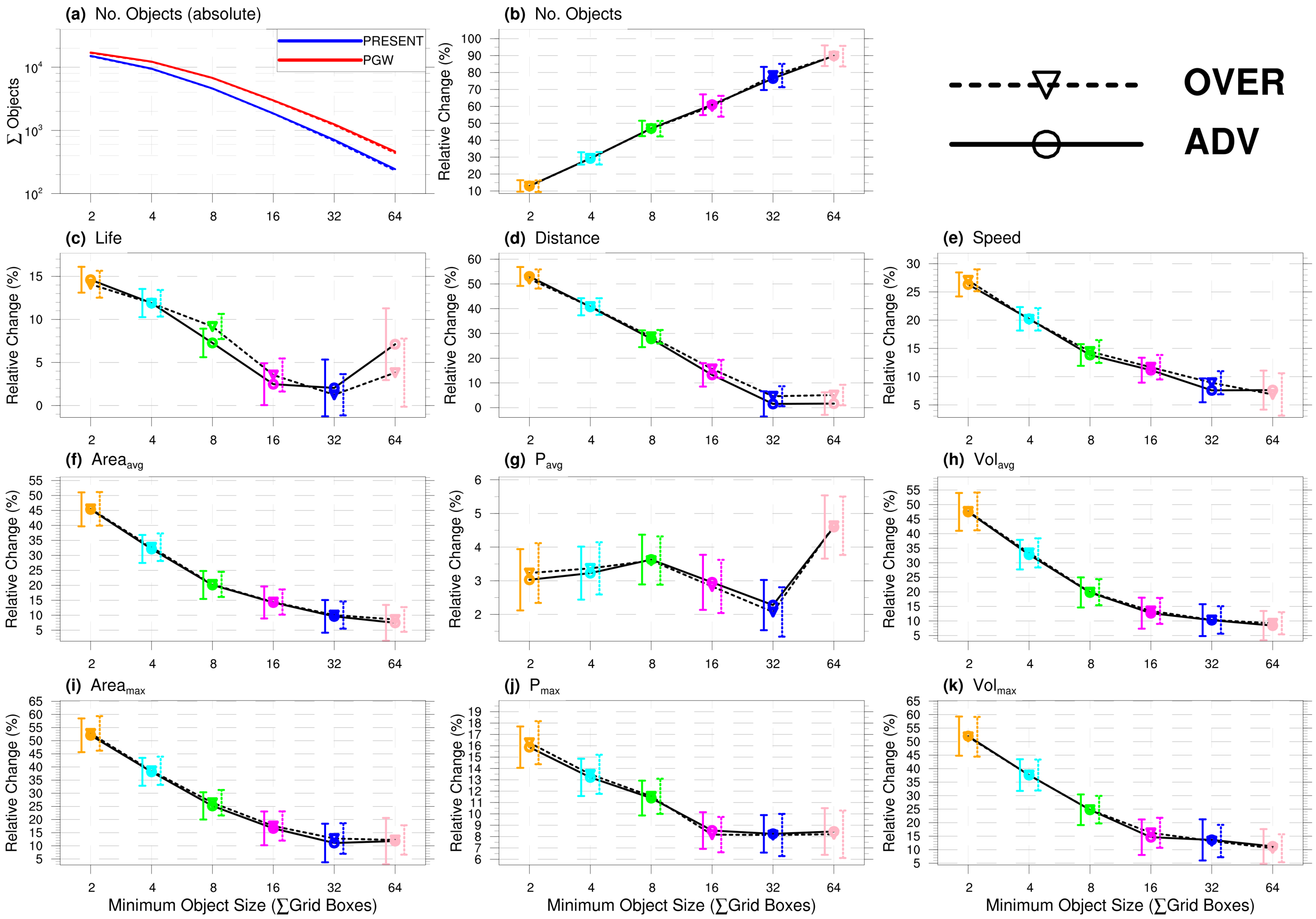

Figure S13: As in Fig. 4 of the main manuscript, i.e. varying A_{min}, except for the 0.9-quantile of each object property.

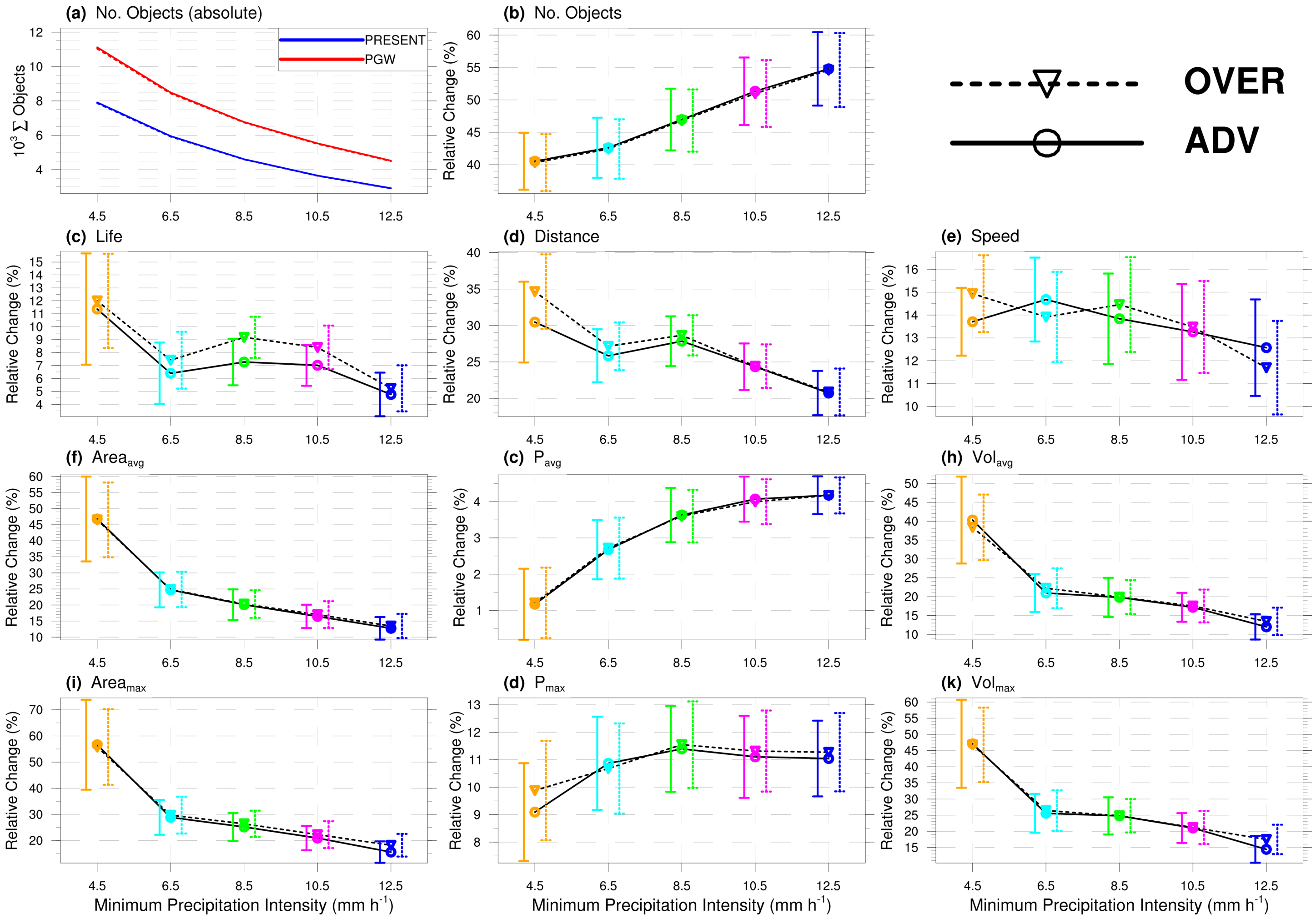

Figure S14: As in Fig. 5 of the main manuscript and Fig. S3, i.e. varying P_{min}, except for the 0.9-quantile of each object property.

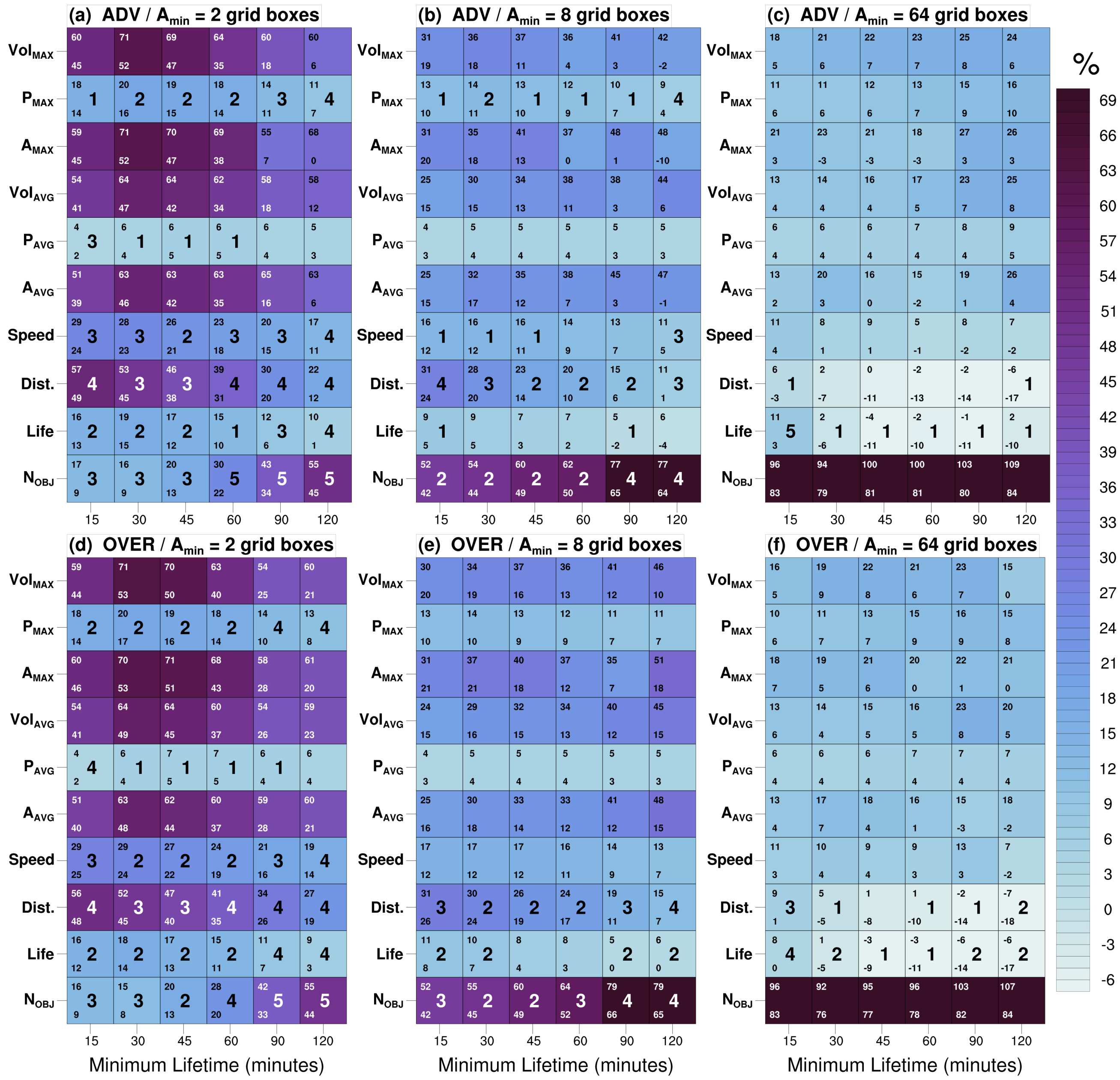

Figure S15: As in Fig. 6 of the main manuscript, i.e. varying T_{min}, except for the 0.9-quantile of each object property.

References

E. P. Meredith, H. W. Rust, and U. Ulbrich. A classification algorithm for selective dynamical downscaling of precipitation extremes. *Hydrology and Earth System Sciences*, 22(8):4183–4200, 2018. doi: 10.5194/hess-22-4183-2018. URL `https://www.hydrol-earth-syst-sci.net/22/4183/2018/`.

E. P. Meredith, U. Ulbrich, and H. W. Rust. The Diurnal Nature of Future Extreme Precipitation Intensification. *Geophysical Research Letters*, 46(13):7680–7689, 2019. doi: 10.1029/2019GL082385. URL `https://agupubs.onlinelibrary.wiley.com/doi/abs/10.1029/2019GL082385`.

E. P. Meredith, U. Ulbrich, H. W. Rust, and H. Truhetz. Present and future diurnal hourly precipitation in 0.11° EURO-CORDEX models and at convection-permitting resolution. *Environmental Research Communications*, 3(5):055002, 2021. doi: 10.1088/2515-7620/abf15e.